# 1

# History and Status of the CAFM

*Chengbin Pan, Yuanyuan Shi, Fei Hui, Enric Grustan-Gutierrez, and Mario Lanza*

*Soochow University, Collaborative Innovation Center of Suzhou Nanoscience and Technology, Institute of Functional Nano & Soft Materials (FUNSOM), 199 Ren-Ai Road, Suzhou 215123, China*

## 1.1 The Atomic Force Microscope

The atomic force microscope (AFM, Figure 1.1) measures the interaction force that appears between an ultrasharp tip and a sample when the distance separating them is in the nanometric range [1]. The tip, which at the apex has a radius down to few nanometers, is located at the end of a cantilever. Its length, width, and thickness are typically of hundreds, tens, and few micrometers (respectively) [2]. The interaction force between the tip and the sample ($F_c$) produces a deflection of the cantilever according to Hooke's law [3] (see Eq. (1.1)), where $k_c$ and $\delta_c$ are the spring constant and the deflection of the cantilever.

$$F_c = -k_c \cdot \delta_c \tag{1.1}$$

In most AFMs, this deflection is detected using an optical system based on a laser beam focused on the top surface of the cantilever driving the reflection to the center of a photodiode (see Figure 1.2) [4]. When the tip is far from the surface, the interaction between tip and sample is null and, therefore, no deflection of the cantilever is observed (the laser spot stays at the center of the photodiode). When the tip is close enough to the sample, the cantilever flexes due to the interaction force that appears between both of them, and the laser spot is deflected, changing its position on the photodiode. By processing the position of the laser spot on the photodiode, the force that has provoked such deflection can be quantified. Since the force depends on the distance that the tip has deflected (Eq. (1.1)), information about the topography of the analyzed sample can be obtained. Following this working principle, if the AFM tip is moved laterally along the surface of the sample (in the $X$ and $Y$ axes), topographic information about an entire area (many point locations) can be collected. These data are sent to the computer which, using an image processing software, can depict a three-dimensional (3D) topographic map [5]. Usually a standard AFM topographic map contains a matrix of $256 \times 256$ pixels (positions). The number of lines per image and pixels per line, as well as many other live scan parameters, such as tip lateral speed, can be easily modified via software.

*Conductive Atomic Force Microscopy: Applications in Nanomaterials,* First Edition.
Edited by Mario Lanza.
© 2017 Wiley-VCH Verlag GmbH & Co. KGaA. Published 2017 by Wiley-VCH Verlag GmbH & Co. KGaA.

**Figure 1.1** Photograph of the dimension icon AFM from Bruker. This is the most representative image of an AFM, as this equipment (and previous models with very similar structure) are by far the most widespread (sold) AFM configuration. (Reproduced with permission from [1]. Copyright Bruker 2015.)

However, this methodology entails certain risks: if the tip scans at a constant height in the $Z$-axis the presence of a high hillock on the surface of the sample can result in a dramatic collision, leading to unwanted tip/sample damage. Similarly, if the tip encounters a deep enough valley on the sample, the distance between them may become too large, leading to negligible tip/sample interaction and therefore failure to monitor the topography of the sample. To avoid these problems, the AFM uses an electronic feedback (controller) that continuously corrects the tip-to-sample distance in the $Z$-axis after measuring the height of each pixel (location) within the image (map), ensuring constant cantilever deflection during the whole scan [3] (see Figure 1.2). The cantilever deflection (also called the *deflection setpoint*) can be set by the user via software, and it controls the interaction force between the tip and the sample. The movement of

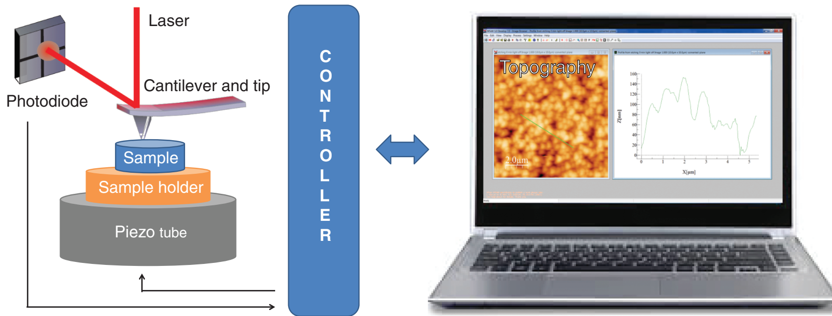


**Figure 1.2** Schematic displaying how the cantilever deflections in an AFM can be processed to obtain a topographic map. The deflection of the cantilever is detected with a laser, and the changes of the laser position in the photodiode are sent to the controller which corrects the position of the tip through the piezo tube. The data are used to build a topographic map using an image processing software compatible with AFMs. (Modified and reprinted with permission from [4], copyright by Jelena Živković 2013.)

the tip and/or sample in the $X$, $Y$, and $Z$ directions is normally applied through piezoelectric actuators. Most AFMs incorporate a piezotube that provides 3D movement to the tip and/or the sample (in Figure 1.2 it moves the sample). The AFM also requires a mechanical anti-vibration system that isolates it from external perturbations. This allow the AFM achieving a resolution down to 1 nm in the $X$, $Y$-directions and 0.1 nm in the $Z$-direction.

It is worth noting that some modern AFMs do not use an optical system (laser plus photodiode) to detect the changes on the tip deflection, instead they use a piezoelectric sensor attached to the cantilever. When the cantilever flexes, the resistance of the piezoelectric sensor changes quantifying the surface height. This system, called *tuning fork* [6], avoids mounting any hardware above the tip (e.g., photodiode) leading to an easy combination with other tools (e.g., Raman spectroscopy), as well as multiprobe configurations. This setup is analyzed in depth in Chapter 13.

Depending on the tip-sample distance during the measurements, different operation regimes can be described. For distances larger than 0.5 nm, the detected forces are mainly electrostatic, magnetic, and van der Waals, which result in an attractive regime [7, 8]. On the contrary, for distances smaller than 0.3 nm, the tip-sample interaction turns into a repulsive regime, in which it can be considered that the tip physically contacts the sample. The contact area between the tip and the sample ($A_c$) mainly depends on the contact force, the geometry of the tip, and the stiffness of both tip and sample, and it is widely accepted that it can range between 1 and 800 nm$^2$ [9, 10] (see also Chapter 3). Both operation regimes lead to the two classic operation modes of an AFM: the contact and the noncontact modes. The main difference between them is that in contact mode the vertical resolution is higher but, on the other hand, the lateral frictions with the surface of the sample are much larger, leading to undesired tip and/or sample wearing. Some alternative operation modes that combine the benefits from both of them (e.g., the tapping mode) [11] have been developed.

Finally, it is important to take into account that, when the AFM measurements are performed in air (without any environmental control system), a water layer gets deposited on the surface of both the tip and the sample owing to the ambient humidity. This water layer, which acts as a meniscus when the tip contacts the surface, introduces capillary forces between the tip and the sample, which must be also considered [12].

## 1.2 The Conductive Atomic Force Microscope

The conductive AFM (CAFM), also referred to in the literature as C-AFM, conductive probe AFM (CP-AFM), conductive scanning probe microscope (C-SPM), or conductive scanning force microscope (C-SFM), is basically an AFM that records the currents flowing at the tip/sample nanojunction simultaneously to the topography. The structure of a CAFM (see Figure 1.3) is very similar to that of the standard AFM, with only three main differences: (i) the probe tip must be conductive, (ii) a voltage source is needed to apply a potential difference between the tip and the sample holder, and (iii) a preamplifier is used to convert the (analogical) current signal into (digital) voltages that can be read by the computer. CAFM probes can be easily acquired from any manufacturer at competitive prices [2], the voltage source is located inside the AFM controller (no additional hardware is required), and the preamplifier can be purchased from the AFM manufacturer. In CAFM experiments, the sample is usually fixed on the sample holder using a conductive tape or paste, the most widely used being silver paints [13]. A Faraday cage is also convenient to isolate the sample from any external electrical interference. Using this setup, when a potential difference is imposed between the tip and the sample an electrical field is generated, which results in a net current flowing from the tip to the sample or vice versa. Therefore, the local electrical properties of the samples can be monitored at a very high nanometric resolution. The currents collected by the CAFM obey Eq. (1.2) [14], in which $I$ is the total current flowing through the tip/sample nanojunction, $J$ is the current density, and $A_{eff}$ is the effective emission area

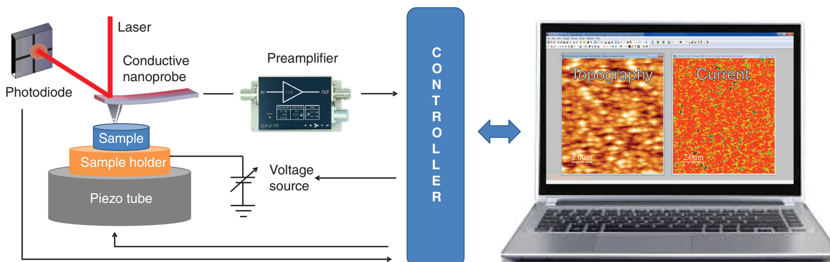


**Figure 1.3** Block diagram of a conventional conductive atomic force microscope. Compared to the AFM, the three new elements are the conductive tip, preamplifier, and sample bias.

through which electrons can flow (from now on we will refer to it just as effective area).

$$I = J \cdot A_{\text{eff}} \tag{1.2}$$

The value of $J$ mainly depends on the conductivity of the tip/sample system and the voltage applied between them, and it is highly affected by intrinsic inhomogeneities in the samples, such as thickness fluctuations, local defects, and doping. The lateral resolution of the technique is defined by the term $A_{\text{eff}}$, which can range from tenths of square nanometers up to thousands of square micrometers depending on many experimental factors, including the conductivity of the sample, the geometry of the tip, the tip/sample contact force, the stiffness of the tip and the sample, and even the relative humidity of the atmosphere in which the experiment is performed.

The most common mistake in CAFM research is to assume that the effective emission area ($A_{\text{eff}}$) equals the physical contact area ($A_c$). Strictly, this assumption is erroneous because in many different tip/sample systems, the electrical field applied may propagate laterally (see Figure 1.4). For example, when the CAFM tip is placed on a metallic electrode, $A_{\text{eff}}$ equals the entire area covered by the electrode, as its lateral electrical conductivity is very high [15, 16]. In order to provide a comprehensive definition, the effective area $A_{\text{eff}}$ can be understood as the sum of all those infinitesimal spatial locations on the surface of the sample that are electrically connected to the CAFM tip (the potential difference is negligible). As such, $A_{\text{eff}}$ is a virtual entity that summarizes all electrically relevant effects within the tip/sample contact system into a single value, over which the current density is assumed to be constant. The difference between contact area and effective emission area is explained in depth in Chapters 3 and 4. The small

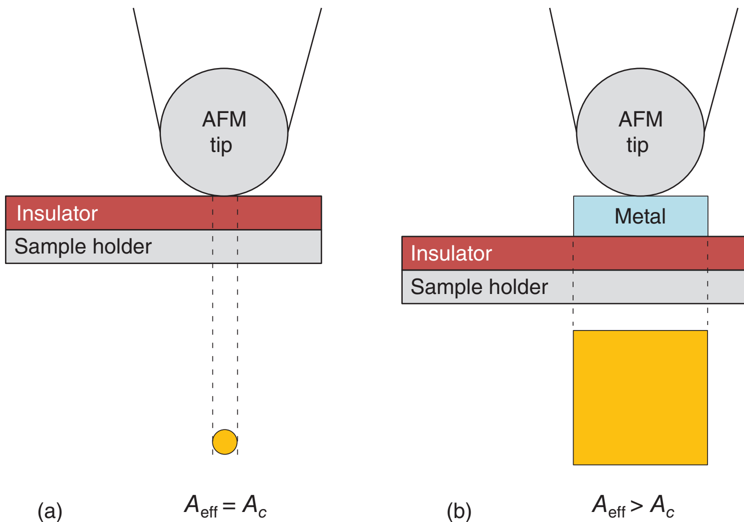


**Figure 1.4** Schematic of the effective emission area through which electrons can flow ($A_{\text{eff}}$) in a CAFM when the tip is placed on (a) a flat insulating sample and (b) a flat metallic electrode deposited on an insulating sample.

dimensions of $A_{eff}$ make the current densities flowing through the tip/sample system extremely large. The smallest currents detected by a CAFM are defined by its electrical noise, which is (in the best cases) hundreds of femtoamperes. A 1 pA current flowing through a typical $A_{eff}$ of 100 nm$^2$ gives a current density of 1 A/cm$^2$. Such large current densities can dramatically accelerate the degradation of most CAFM probe tips, reducing the reliability of the measurements and increasing the cost of the research. This problem is further aggravated by the high lateral frictions present in the tip/sample system during the scans [17, 18].

The first types of conductive nanoprobes used in CAFM experiments, which are still widely used nowadays, are the standard silicon nanoprobes varnished with thin metallic films, including Pt, Au, Ru, Ti, and/or Cr (Figure 1.5). The thickness of the varnish should be thick enough to withstand the large current densities and frictions, and at the same time thin enough to not increase significantly the radius of the tip apex, maintaining its sharpness and ensuring a high lateral resolution during the measurements. As mentioned, the lifetime of conductive tips for CAFM experiments is much shorter than in any other AFM mode, mainly owing to metallic varnish melting and loss of tip mass during the scans. To solve this problem, new CAFM silicon tips coated with hard materials (e.g., phosphorous-doped diamond [19] and graphene [17, 18, 20–24]), as well as full conductive tips [25–27] have appeared (see Figure 1.5). Other factors related to the sample, such as stiffness, rugosity, stickiness, and conductivity play very important roles when deciding on the type of tip to be used in a CAFM analysis. Chapter 2 presents an in-depth description of the fabrication process and reliability of conductive nanoprobes for AFM. Advices on how to select the best CAFM tip for each experiment are provided in Chapter 2.

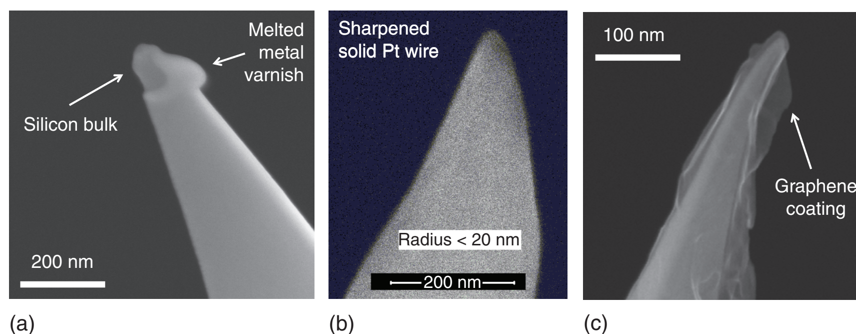


**Figure 1.5** (a) Scanning electron microscope images of (a) metal-varnished silicon nanoprobe, (b) a sharpened solid Pt wire compatible for CAFMs, and (c) a metal-varnished silicon nanoprobe coated with a sheet of single-layer graphene. The picture in (a) intentionally shows a tip with the metallic varnish worn off, so that the core bulk of silicon can be observed. (Panels (a) and (c) have been modified and reprinted with permission from [18], copyright from Royal Society of Chemistry 2016. Panel (b) has been reproduced with permission from [25], copyright American Institute of Physics 2004.)

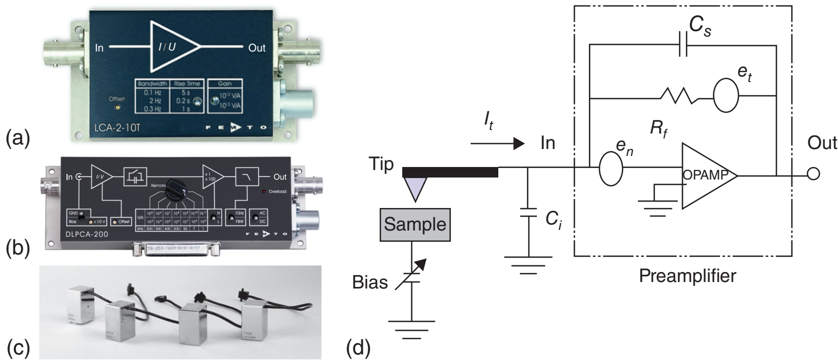


**Figure 1.6** (a, b) Photographs of two preamplifiers for CAFMs, the first one with fixed gain and the second with variable gain. (c) Photographs of different application modules for Bruker AFMs, including the CAFM module (which contains a preamplifier). (d) Simplified schematic of a conventional preamplifier used in CAFMs. The main parts are (i) an operational amplifier with high input impedance (OPAMP); (ii) a feedback resistor ($R_f$) and its parasite capacitor ($C_s$) and Johnson noise ($e_t$)-associated effects; (iii) a noise voltage source associated with the operational amplifier ($e_n$); and (iv) a capacitance associated with the input interconnections ($C_i$). (Panels (a) and (b) have been reprinted from [29], copyright FEMTO 2015. Panel (d) has been modified and reprinted with permission from [30], copyright American Institute of Physics 1990.)

The analogical current signals flowing through the tip/sample nanojunction are sent to the preamplifier Figure 1.6a,b, which transforms them into digital voltages that can be read by the data acquisition (DAQ) card of the computer (see Figure 1.6). Many manufacturers integrate the preamplifier in the so called "CAFM application module," which is a removable component that can be fixed to the AFM (usually very close to the tip to minimize electrical noise). Similarly, many other modules allow AFMs to perform other operations (see Figure 1.6c), such as scanning capacitance microscopy (SCM) or scanning spreading resistance microscopy (SSRM). In most CAFM experiments, the currents measured can range typically from few picoamperes to hundreds of microamperes, while the voltages readable by the DAQ card usually range between −3 and +3 V [31]. Therefore, the preamplifier needs to provide a very low noise and a high transimpedance (gain). Figure 1.6d shows the simplified schematic of a typical low-noise preamplifier for CAFM measurements [30], in which some elements can be distinguished: (i) an operational amplifier with high input impedance; (ii) a feedback resistor ($R_f$) and its parasite capacitor ($C_s$) and Johnson noise ($e_t$)-associated effects; (iii) a noise voltage source associated with the operational amplifier ($e_n$); and (iv) a capacitance associated with the input interconnections ($C_i$). A correct selection of the electrical components is essential to achieve good and reliable CAFM data acquisition. For example, the value of $R_f$ is not trivial: a very high value of $R_f$ improves the noise-signal ratio, while reduces the bandwidth of the preamplifier. Therefore, the value of $R_f$ should

be chosen to provide enough bandwidth and a noise level below the current values that we want to measure. The parameter $e_n$ can be easily reduced by using a commercial low-noise operational amplifier. The capacitance associated with the connections ($C_i$) can be easily minimized by placing the preamplifier as near as possible to the conductive tip. The company FEMTO, one of the world's leading manufacturers of preamplifiers compatible with CAFMs, can provide devices with electrical noise as low as 3 fA and a gain up to $10^{13}$ V/A [29] (similar to those in Figures 1.6). Nevertheless, the main limitation of CAFM preamplifiers is their narrow current dynamic range, which usually allows collecting electrical signals only within three or four orders of magnitude (or even less). To solve this problem, preamplifiers with an adjustable gain can be used to focus on specific ranges [29] (similar to the one in Figure 1.6b). A more sophisticated solution for this problem is to combine the CAFM with a sourcemeter [17, 18], semiconductor parameter analyzer (SPA), or with a logarithmic preamplifier [28], which can capture the currents flowing through the tip/sample system at any range and with a high resolution. These methodologies are amply described in Chapters 10–12.

The currents flowing through the tip/sample system and converted by the preamplifier are (in almost every CAFM experiment) a consequence of the application of a voltage between the tip and the sample holder. Only a small portion of the works reported with CAFM did not require the application of a bias, that is, in the case of experiments in which the current is generated by other means, such as photoelectric [32] or piezoelectric [33] effects. Most CAFMs let the user select the value and polarity of the bias which should be applied on the tip while keeping the sample holder grounded, or vice versa. Therefore, the currents usually flow vertically through the sample [10], although lateral currents can be also measured by connecting the surface of the sample to the sample holder [34] (e.g., using silver paint or a wire bonder). Usually CAFM electronics allow applying voltages ranging from −10 to +10 V and, as mentioned, the currents that can be observed are always within three or four orders of magnitude, never smaller than 1 pA or larger than 10 μA. Apart from constant voltage stresses (CVS) applied during a scan, ramped voltage stresses (RVS) to collect current versus voltage ($I$–$V$) curves can also be performed by keeping the tip static at one single location (during the RVS). Despite this setup being more than enough for many experiments, some studies may require the use of enhanced electronic capabilities, such as the application of constant current stresses (CCS), the measurement of current versus time curves ($I$–$t$), the use of current limitations, or simply the application or measurement of larger voltages or currents. Many AFMs incorporate an input/output directly connected to the tip or the sample holder (or even both), allowing the use of an external sourcemeter or an SPA to apply/collect electrical signals. A detailed description of the combination of CAFM with a sourcemeter and SPA is presented in Chapter 10.

With this setup, many different kinds of experiments have been performed in recent years. The CAFM can be used to monitor the properties of materials, as well as to modify them with atomic resolution.

## 1.3 History and Status of the CAFM

While the first AFM was developed by G. Binning, C. F. Quate, and C. H. Gerber in 1886 at the IBM Research Laboratories in Zurich [35], the first modification of an AFM to perform current measurements was reported by M. P. Murrel at the Engineering Department of Cambridge University [36] in 1993. The setup was initially conceived to monitor local tunneling currents through 12 nm thick $SiO_2$ films. The authors evaporated 100 nm of titanium on a standard silicon cantilever from Nanoprobe, and monitored the current flowing from the sample to the tip using a picoammeter and a homemade digital-signal-processor-based AFM control system. The experiment consisted of measuring an $I$–$V$ curve at different locations on the sample (Figure 1.7a) distributed in a matrix form. By reporting the voltages at which tunneling current appeared at each location, the authors built up the first AFM image containing electrical information about the analyzed sample (each location represents a pixel of the image, Figure 1.7b). The data unequivocally show local variations of the conductivity in the $SiO_2$ film. By fitting the currents measured during the $I$–$V$ curves to the Fowler-Nordheim equation, the authors reported for the first time the value of $A_{eff}$, which was in that case $500 \pm 500\ nm^2$, and they suggested a lateral resolution below 20 nm.

Over the following years, the CAFM became a very popular tool in the field of characterization of thin dielectrics. In 1995 and 1996, O'Shea *et al.* [37] and Ruskell *et al.* [38] further improved the lateral resolution of the CAFM technique, achieving values of 10 and 8 nm, respectively. This enhanced resolution allowed to observe the first topographic–current correlations, and the inhomogeneity

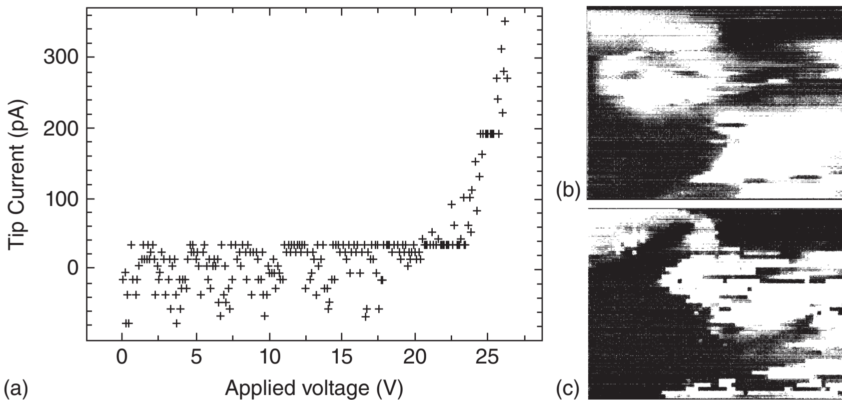


**Figure 1.7** (a) First $I$–$V$ curve measured with a CAFM. The sample was a 20 nm thick $SiO_2$ film grown on silicon. (b) Tunneling voltage image over an area 450 nm × 330 nm. The contrast is proportional to the threshold voltage required at each image point to generate a tunnel current of 0 pA. White to black corresponds to applied voltages of 15.0 and 40.5 V, respectively. (c) AFM topography of oxide surface recorded in the repulsive mode. Black to white correspond to a total vertical excursion of 90 nm. (Reprinted from [36]. Copyright American Institute of Physics.)

observed in the current maps was associated with the presence of local native defects in the oxide. Works by Olbrich [39–41] and Ebersberger [42] reported that, in $SiO_2$ films thinner than 5 nm, the tunneling current increases exponentially with thickness reductions. Consequently, thickness fluctuations of tenths of nanometer in the $SiO_2$ film could create electrically weak spots that reduce the reliability of the whole dielectric film, as dielectric breakdown (BD) is a stochastic process. The capability of the CAFM for determining the thickness of thin oxides was further demonstrated by Frammelsberger and co-workers [10, 43] who statistically analyzed more than 7200 $I$–$V$ curves, and reported $SiO_2$ thicknesses with a sensitivity of ±0.3 nm. Other local phenomena such as charge trapping [44], trap-assisted tunneling [45–50], and stress-induced leakage current (SILC) [51] can be also easily monitored with CAFM. In general, the CAFM can monitor the effect of any process that introduces local changes in the structure of the dielectric, including thermal annealing [52–58], doping [59], and irradiation [60–62].

In particular, the CAFM is especially useful to determine which locations of the samples lead to premature BD, which can provide essential information about the reliability of the samples. In this direction, Iglesias *et al*. [63] demonstrated that in 5-nm-thick polycrystalline hafnium dioxide the grain boundaries are weaker from an electrical point of view, presenting larger currents in current maps (see Figure 1.8), and that the BD is potentially triggered with more ease in these sites. The images displayed in Figure 1.8 show unprecedented high resolution and topography-current correlation, as they were performed in ultrahigh vacuum (UHV) conditions (see Chapter 3). The CAFM also helped to confirm the percolation theory of the BD by experimentally proving that this is a very local phenomenon that occurs in small areas typically below 100 $nm^2$ [51]. Lateral propagations of the BD event can also be detected by CAFM [64–66]. By using an external SPA connected to the CAFM, the relationship between the current limitation and the size of the BD spot can also be assessed [67, 68], and the statistical analyses of these nanoscale data also fit the same distributions (Weibull) as those at the device level [69, 70]. The severity of the BD event

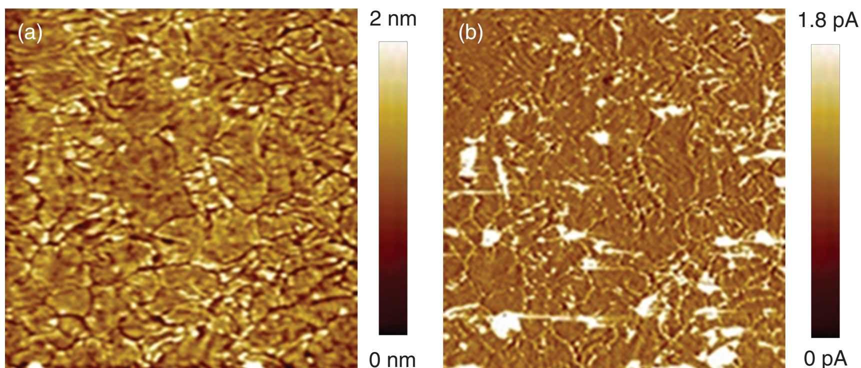


**Figure 1.8** (a) Topographical and (b) current images obtained at 6.5 V on the surface of a polycrystalline $HfO_2/SiO_2/Si$ stack (area 1 μm × 1 μm. The CAFM revealed that the crystals are more insulating than the grain boundaries. (Reprinted with permission of [63]. Copyright American Institute of Physics 2010.)

can also be studied from the BD-induced epitaxy [45, 71–73], which can be observed in subsequent topographic images collected with the CAFM after a voltage ramp. Similarly, the analysis of the BD recovery (resistive switching RS) can also be monitored by CAFM. In 2012, it was widely accepted that transition metal oxides such as $HfO_2$, $Al_2O_3$, and $TiO_2$ could show RS, enabling their use in resistive random access memories but the physics behind the RS phenomenon and the local features promoting this behavior were still unknown. By using a CAFM, Lanza *et al.* [74] demonstrated for the first time that, in atomic-layer-deposited $HfO_2$ films, RS only takes place at the grain boundaries of polycrystalline samples. All the capabilities of the CAFM for studying RS in dielectrics have been summarized in the review article of Ref. [75].

The use of CAFM for the characterization of thin dielectrics has been recently also extended to the field of 2D dielectrics. Lee *et al.* [76] analyzed for the first time the tunneling current through multilayer hexagonal boron nitride (*h*-BN) sheets using a CAFM. More specifically, he reported that the leakage current at low fields in *h*-BN thinner than three layers occurs by direct tunneling, while in thicker stacks it flows according to the Fowler-Nordheim tunneling. In fact, the CAFM has become very useful in these early stages of 2D materials research as they were firstly isolated by mechanical exfoliation, and the size of the nanosheets produced by this method is too small to place electrodes by photolithography (i.e., they can only be electrically characterized via CAFM). Ji *et al.* [77] analyzed the degradation process of multilayer *h*-BN and, by measuring sequences of CAFM $I$–$V$ curves she determined that *h*-BN is much more reliable than $HfO_2$ films with similar equivalent oxide thicknesses. Hattori *et al.* [78] analyzed the BD event in multilayer *h*-BN and, by combining $I$–$V$ curves with topographic/current maps, he determined that the BD takes place layer by layer. These properties of *h*-BN could be only obtained thanks to the capabilities of the CAFM [79, 80].

Apart from the study of thick dielectrics, the CAFM technique has expanded to many other fields of science, including physics, materials science, chemistry, and engineering. Table 1.1 classifies the number of CAFM-related papers (and their citations) in the main different fields of science. As can be seen, the CAFM has been successfully used to study nanoparticles [81], molecules [82], nanowires (NW) [33], carbon nanotubes [83], two dimensional materials [63, 84, 85], coatings [86], local oxidation [87], photoelectricity [88], and piezoelectricity [89]. In general, CAFM can be a very powerful technique to acquire valuable local electrical information of any kind of sample or device, and for this reason, CAFM research has spread rapidly. Since its invention in 1993 and as of June 14, 2016, the total number of CAFM-related research papers detected in the Web of Science[1] is 1618 [90], and Figure 1.9 shows the number of research papers published per year (and their citations). According to the number of citations, Table 1.2

1 Search criteria used: "Topic" = "conductive atomic force microscopy" or "conductive atomic force microscope" or "conducting atomic-force microscopy" or "conducting atomic-force microscope" or "conductive AFM" or "conductive-AFM" or "conductive probe AFM" or "conductiveprobe atomic force microscope" or "conductive probe atomic force microscopy" or "conductive scanning probe microscope" or "conductive scanning probe microscopy" or "conductive scanning force microscope" or "conductive scanning force microscopy" or "local conductive atomic force microscope" or "local conductive atomic force microscopy" or "local conductive AFM" or "LC-AFM."

**Table 1.1** Research area rankings in CAFM publications.

| Research area | Number of papers | Citations |
|---|---|---|
| Physics | 1 106 | 18 824 |
| Materials science | 702 | 12 080 |
| Science, technology, other topics | 511 | 12 832 |
| Chemistry | 439 | 11 252 |
| Engineering | 214 | 2 130 |
| Microscopy | 81 | 1 678 |
| Electrochemistry | 62 | 1 024 |
| Optics | 53 | 523 |
| Biochemistry, molecular biology | 51 | 1 389 |
| Physiology | 47 | 1 559 |

*Source:* Thomson Reuters ISI Web of Science; search dated June 14, 2016 using "Topic" = "conductive atomic force microscopy" or "conductive atomic force microscope" or "conducting atomic-force microscopy" or "conducting atomic-force microscope" or "conductive AFM" or "conductive-AFM" or "conductive probe AFM" or "conductive probe atomic force microscope" or "conductive probe atomic force microscopy" or "conductive scanning probe microscope" or "conductive scanning probe microscopy" or "conductive scanning force microscope" or "conductive scanning force microscopy" or "local conductive atomic force microscope" or "local conductive atomic force microscopy" or "local conductive AFM" or "LC-AFM."

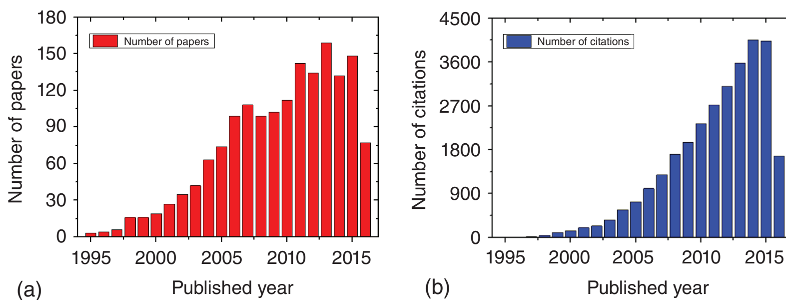


**Figure 1.9** Statistic analysis of the (a) publication number and (b) citation about CAFM in each year (Thomson Reuters ISI Web of Science; search dated September 20, 2015 using "Topic" = "conductive atomic force microscope" or "conductive atomic force microscopy" or "conducting atomic-force microscopy" or "conductive AFM"; 1325 records).

compiles the most influential research papers in CAFM research, and Table 1.3 shows the ranking of the most active countries in CAFM research, on the basis of the number of publications.

One of the main reasons for the versatility of the CAFM is the continuous development of commercial setups with enhanced capabilities. For example, the Veeco DI 3100 AFM (and its newer evolution, the Bruker's Dimension Icon®) provides a genuine large-size sample holder that remarkably reduces the setup preparation time if many samples need to be studied [91]. Oxford Instruments

**Table 1.2** Paper citation rankings in CAFM publications.

| Title | Author | Reference | Citations |
|---|---|---|---|
| Piezoelectric nanogenerators based on zinc oxide nanowire arrays | Z. L. Wang and J. H. Song | *Science*, **312**, 242–246, 2006 | 3077 |
| Switching the electrical resistance of individual dislocations in single-crystalline $SrTiO_3$ | K. Szot, W. Speier, G. Bihlmayer, and R. Waser | *Nat. Mater.*, **5**, 312–320, 2006 | 915 |
| Resistive switching mechanism of $TiO_2$ thin films grown by atomic-layer deposition | B. J. Choi, D. S. Jeong, S. K. Kim, C. Rohde, S. Choi, J. H. Oh, H. J. Kim, C. S. Hwang, K. Szot, R. Waser, B. Reichenberg, and S. Tiedke | *J. Appl. Phys.*, **98**, 033715, 2005 | 681 |
| Conduction at domain walls in oxide multiferroics | J. Seidel, L. W. Martin, Q. He, Q. Zhan, Y.-H. Chu, A. Rother, M. E. Hawkridge, P. Maksymovych, P. Yu, M. Gajek, N. Balke, S. V. Kalinin, S. Gemming, F. Wang, G. Catalan, J. F. Scott, N. A. Spaldin, J. Orenstein, and R. Ramesh | *Nat. Mater.*, **8**, 229–234, 2009 | 455 |
| A bond-fluctuation mechanism for stochastic switching in wired molecules | G. K. Ramachandran, T. J. Hopson,A. M. Rawlett, L. A. Nagahara, A. Primak, and S. M. Lindsay | *Science*, **300**, 1413–1416, 2003 | 341 |
| Nanoscale control of an interfacial metal-insulator transition at room temperature | C. Cen, S. Thiel, G. Hammerl, C. W. Schneider, K. E. Andersen, C. S. Hellberg, J. Mannhart, and J. Levy | *Nat. Mater.*, **7**, 298–302, 2008 | 275 |
| Probing the nature of defects in graphene by Raman spectroscopy | A. Eckmann, A. Felten, A. Mishchenko, L. Britnell, R. Krupke, K. S. Novoselov, and C. Casiraghi | *Nano Lett.*, **12**, 3925–3930, 2012 | 264 |
| Making electrical contacts to molecular monolayers | X. D. Cui, X. Zarate, J. Tomfohr, O. F. Sankey, A. Primak, A. L. Moore, T. A. Moore, D. Gust, G. Harris, and S. M. Lindsay | *Nanotechnology*, **13**, 5–14, 2002 | 256 |
| Electrochemical reduction of oriented fraphene oxide films: an in situ Raman spectroelectrochemical study | G. K. Ramesha and S. Sampath | *J. Phys. Chem. C*, **113**, 7985–7989, 2009 | 254 |

(*continued*)

**Table 1.2** (Continued)

| Title | Author | Reference | Citations |
|---|---|---|---|
| Piezoelectric and semiconducting coupled power generating process of a single ZnO belt/wire. A technology for harvesting electricity from the environment | J. H. Song, J. Zhou, and Z. L. Wang | *Nano Lett.*, **6**, 1656–1662, 2006 | 221 |

*Source:* Thomson Reuters ISI Web of Science; search dated 14 June 2016 using "Topic" = "conductive atomic force microscopy" or "conductive atomic force microscope" or "conducting atomic-force microscopy" or "conducting atomic-force microscope" or "conductive AFM" or "conductive-AFM" or "conductive probe AFM" or "conductive probe atomic force microscope" or "conductive probe atomic force microscopy" or "conductive scanning probe microscope" or "conductive scanning probe microscopy" or "conductive scanning force microscope" or "conductive scanning force microscopy" or "local conductive atomic force microscope" or "local conductive atomic force microscopy" or "local conductive AFM" or "LC-AFM."

**Table 1.3** Country rankings in CAFM publications.

| Country | Number of papers | Citations |
|---|---|---|
| USA | 359 | 13 549 |
| China | 227 | 5 617 |
| Japan | 203 | 2 496 |
| Germany | 167 | 4 331 |
| South Korea | 145 | 2 704 |
| France | 118 | 1 178 |
| Taiwan | 112 | 2 292 |
| Spain | 105 | 1 081 |
| Italy | 101 | 1 224 |
| England | 81 | 2 462 |

*Source:* Thomson Reuters ISI Web of Science; search dated 14 June 2016 using "Topic" = "conductive atomic force microscopy" or "conductive atomic force microscope" or "conducting atomic-force microscopy" or "conducting atomic-force microscope" or "conductive AFM" or "conductive-AFM" or "conductive probe AFM" or "conductive probe atomic force microscope" or "conductive probe atomic force microscopy" or "conductive scanning probe microscope" or "conductive scanning probe microscopy" or "conductive scanning force microscope" or "conductive scanning force microscopy" or "local conductive atomic force microscope" or "local conductive atomic force microscopy" or "local conductive AFM" or "LC-AFM."

(former Omicron) provides AFMs embedded in UHV systems for extremely high accuracy [67, 68] and spatial resolution [63, 92]. Uppal *et al.* [68] studied the pre- and post-degradation of $HfO_2$ dielectrics using an Omicron CAFM working in UHV, and observed a change in the conduction from Fowler-Nordheim to direct tunneling. When measuring electrical currents with the AFM tip, the *Resiscope* mode of Agilent AFMs provides unique extra-large voltage and current dynamic ranges thanks to its logarithmic current-to-voltage converter [93]. This provides a current window up to nine orders of magnitude (from picoamperes to milliamperes), while the electronics of most commercial AFMs saturate around some nanoamperes. Coll *et al.* [94] used this setup to monitor the hysteretic bipolar switching phenomenon in ultrathin $CeO_2$ layers grown on $La_{0.7}Sr_{0.3}MnO_3/SrTiO_3$ functional complex oxides. Newer manufacturers often provide modular structures compatible with other techniques. Stahl *et al.* [95] mounted an AFM head on the sample stage of a commercial SEM (Jeol JSM-820) to prove the functioning of piezoresistive cantilevers. Anderson [96] combined a Digital Instruments AFM with a Kaiser HoloProbe Raman instrument to enhance the Raman signal at the surface of a $C_{60}$ film solution cast on mica. Another interesting mode offered by many manufacturers is the possibility to collect current measuring in semicontact mode, which reduces notably the tip/sample frictions enhancing the lifetime of the tip and the reliability of the samples (see Chapter 3); this methodology also enables the use of the CAFM to study the electrical properties of soft materials such as polymers. The ultimate evolution of the AFM provided by Nanonics incorporates for the first time the possibility to perform multiprobe electrical and optical measurements [97] (up to four probes), thanks to the use of a piezoelectric sensor to detect the deflection of the cantilever [98], avoiding the use of fixed and nonmodular optical detectors (traditional laser and photodiode). This setup is discussed in detail in Chapter 13. Despite these advances, each one of these AFMs presents some important limitations. For example, the Dimension Icon measurements does not provide environmental chamber impeding to perform specific experiments, such as bipolar measurements in many kinds of samples (due to the apparition of local anodic oxidation); Omicron AFMs are complex, as they require long times to prepare the setup, and the UHV degrades the ultrasharp tips extremely fast owing to high frictions (the water layer on the surfaces of both tip and sample are removed); from our experience, Agilent AFMs are not so user-friendly and robust compared to the Veeco/Bruker AFMs, and Nanonics AFMs use self-made transparent and flexible cantilevers that are interesting for many applications, but their lateral resolution is usually smaller than that of traditional ultrasharp silicon cantilevers. Similarly, Park AFMs provide a very powerful software that allows a wide range of image processing, but the tip holder for electronic measurements requires soldering. More details about AFM comparatives can be found in review papers and specialized websites [99].

In the following chapters, we have invited selected top CAFM scientists to describe their work in different CAFM research fields that have had a special impact, not only case studies but also setup developments and their applications.

## 1.4 Editor's Choice: On the Use of CAFM to Study Nanogenerators Based on Nanowires

In this section, we present the use of CAFM for the investigation of piezoelectric NWs. The reason is that this work has had a special impact in nanosciences (see Table 1.2). The use of NWs for energy applications has garnered much attention during the last decade. For example, the fabrication of NWs has been a technique often used to enhance the surface area of a material, which can be beneficial in many energy conversion systems, such as photovoltaic systems [100] and photoelectrochemical water splitting solar cells [101]. In this kind of samples, the CAFM can be a powerful tool to analyze locally the currents generated by the NWs. For example, Pan *et al*. [89] used a standard CAFM to analyze local photo currents generated in arrays of vertically aligned ZnO NWs. Different samples were fabricated, and different performances were detected depending on the amount and size of the NWs clusters, which can be controlled with the insertion a polymer layer between the NWs. NW clustering reduces the light absorbed by the NWs. CAFM contributed to demonstrate that samples without nanoclusters produced larger photocurrents, observing more conductive spots with larger conductivity. Moreover, the currents collected strongly depended on the amount of light driven to the surface of the samples (i.e., percentage of power of the solar simulator). When studying photocurrents, it should be highlighted that the laser of the CAFM can be already used to excite the samples, making easy the observation of photocurrents in the absence of bias. Additional laser illumination could be also used to generate the currents. For example, Howell *et al*. [88] used a CAFM to map the efficiency of GaN/InGaN NW arrays illuminated from the bottom with an additional laser. Through complementing with Raman spectroscopy and finite difference time domain (FDTD) simulations, they noted the influence of NW structure to device performance, confirming that higher indium concentration within the photoactive regions and fewer defects on the NW are able to enhance the cell efficiency. Despite this setup has been also described as scanning photocurrent microscopy (SPCM), the working principle is very similar. It is worth noting that the current collection does not require the application of any bias, confirming the solar-to-electrical energy conversion. More details about how to modify a CAFM for photoelectric applications are given in Chapter 15.

Even more interesting is the characterization of the piezoelectric effect in specific types of NWs, as the tip of the CAFM can at the same time bend the (vertically aligned) NWs while the current is collected. This is a unique capability of the CAFM, as other techniques such as STM do not work in contact mode and, therefore, cannot apply mechanical stresses to the NWs. The first relevant work in this direction was reported in 2006 by Wang and Song [33], who used the CAFM to scan a single and a forest of semiconducting ZnO piezoelectric NWs. To date, a variety of methods have been developed to synthesize piezoelectric NW arrays, including chemical hydrothermal synthesis [102], microwave-assisted hydrothermal synthesis [103], thermal evaporation synthesis [104], vapor-confined face-to-face annealing [105], pulsed direct current magnetron sputtering [106], radiofrequency magnetron sputtering[107],

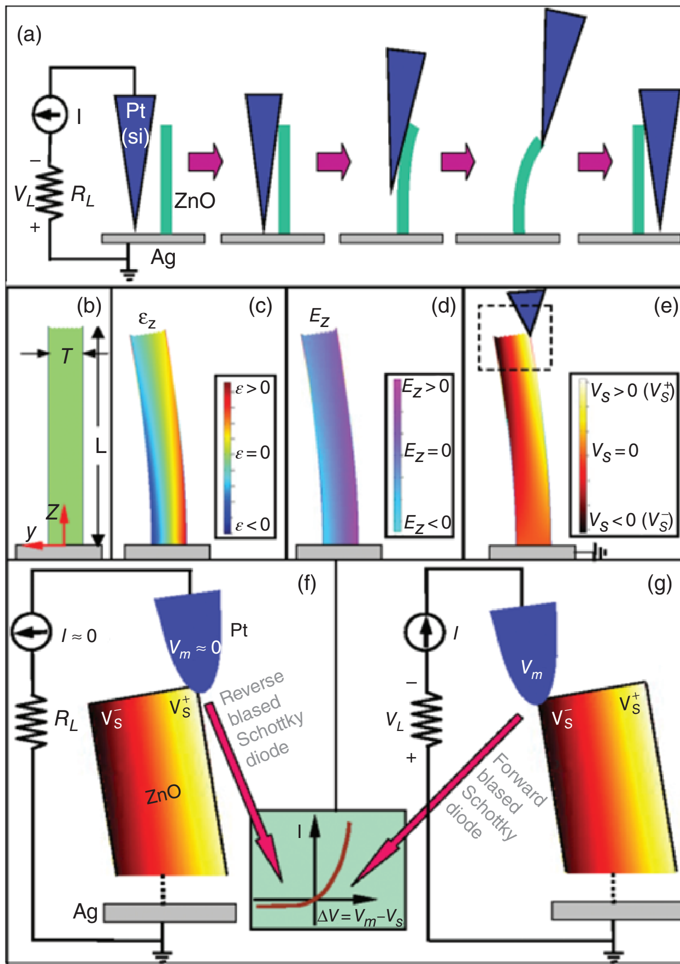


**Figure 1.10** (a) Experimental setup and the whole CAFM measurement procedures in contact mode. (b) Schematic of a freestanding nanowire. (c) Physical strain distribution along the $Z$-axis of the nanowire under transverse stress. (d) Corresponding electrical filed distribution. (e) Coincidentally potential distribution along the tested nanowire. (f, g) Schematic of forward and reversed Schottky barrier respectively.

electron-beam template lithography[108], and chemical vapor deposition[109]. During recent years, chemical hydrothermal synthesis has become a dominant solution owing to its speed, low cost, and operation temperature. In Wang's work [33], the NWs grown by the vapor–liquid–solid (VLS) process were scanned with the CAFM tip as displayed in Figure 1.10, realizing rapidly that, in the absence of bias, current peaks correlated systematically with the bending of the NW. The mechanical strain, and therefore the currents generated, could be controlled by altering the scan parameters such as tip/sample contact force, tip speed and integral/proportional gain. The authors complemented their experimental observations with simulations via finite element method, and reported that

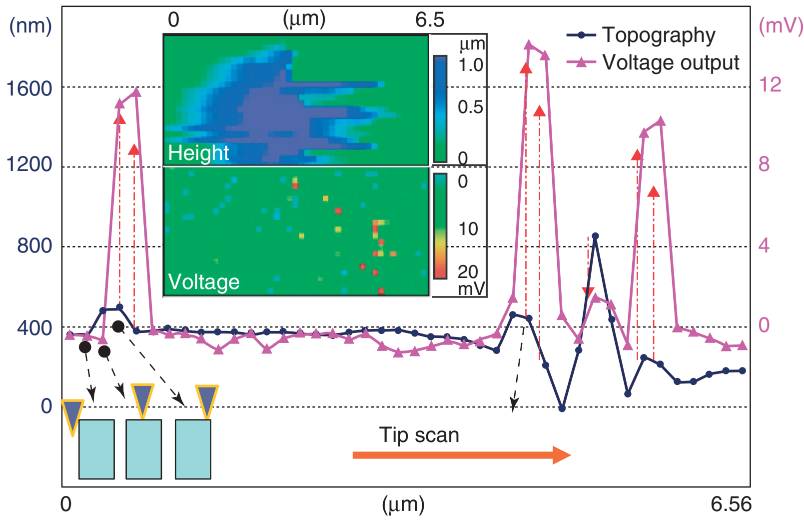


**Figure 1.11** The simultaneously collected profiles of the topograsphy and CAFM current map. The corresponding images of size of 6.5 µm × 3.2 µm are displayed in the inset. A schematic in the left-bottom corner depicts the accurate tip location based on the corresponding cross-section line of topography.

the current is only observable at the compressed surface of the NW, which is forward biased with respect to the (grounded) CAFM tip. From the point of view of energy transformation, during the first half of the bending process, the mechanical energy is first accumulated and stored in the piezoelectric NW. When the tip crosses the neutral line (right at the center of the NW), the stored energy starts to discharge and gradually converts into the electrical current. A detailed description of the experiment is shown in Figure 1.11.

Another behavior that further corroborates the piezoelectric origin of the currents detected is that they appear at different locations of the NW depending on their doping. Su *et al.* [110] observed that p-type GaN semiconducting NWs show the discharge (current peak) when the CAFM tip touches the elongated side of the NW, while for the aforementioned n-type ZnO NWs, that happens on the compressed side (see Figure 1.11). This observations are possible thanks to the unique capability of correlating the topography with the current signals in the CAFM setup. As the NWs usually present a very high aspect ratio, the profile of these structures are particularly easy to monitor. Lanza *et al.* [111] reported very good correlation between topography and current in highly populated arrays of vertically aligned ZnO NWs (Figure 1.12). Yang *et al.* [112] also observed such correlation in similar structures during a single line scan. The relationship between height/width and currents generated can be also studied via CAFM. A sequence of CAFM measurements in piezoelectric nanogenerators based on the GaN NW arrays was carried out by Hung [113]. Vertical n-type GaN NW arrays with different aspect ratios were grown on a GaN sample by inductively coupled plasma etching. Then, these NWs were sequentially scanned with

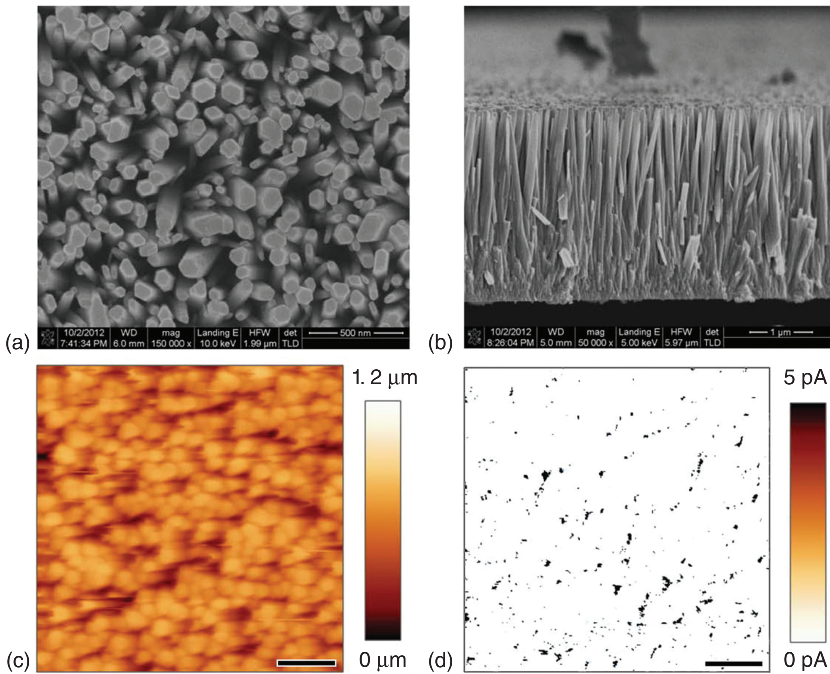


**Figure 1.12** Nanowire characterization. (a, b)Top and cross-sectional SEM images of the nanowire array. (c, d) Simultaneously collected topographic and current maps on the same sample using a Pt-Ir tip exerting a force of 0.1 nN and without bias. The scale bar for images (c, d) is 1 μm.

the CAFM using a conductive CrPt-coated nanoprobe. The measurements indicate that the piezo-current generated by the GaN NW starts to decrease as the aspect ratio increases, and that the output voltage could nearly approach zero when the aspect ratio is close to one.

It is very interesting that the current densities measured at the device level and at the nanoscale in nanogenerators made of piezoelectric NWs are dramatically different. When the NWs array is sandwiched between two electrodes and compressed, the current densities collected (typically using a sourcemeter or an SPA) are very modest, typically of the order of just a few micrometer per square centimeter [114]. On the contrary, the currents collected with the tip of the CAFM for similar structures are of few/tens of picoamperes. Considering the emission area ($A_{eff}$) in CAFM experiments (~100 $nm^2$) that implies a current density of 1 $A/cm^2$ (in the worst case, for a current of just 1 pA). Therefore, the potential for energy conversion of ZnO NWs is uniquely demonstrated thanks to the CAFM. The explanation for this current mismatch is related to the difficulty in driving the current out of the NWs array, as well as due to the formation of NW clusters. The effectiveness of the strategies used to solve this problem can also be studied by means of CAFM. For example, the poor interface between the flat, rigid, top electrode and the vertically aligned NWs can be improved by patterning pyramidal brushes at the bottom interface of the top electrode, which improves the contact

with the NWs [115]. Another more sophisticated methodology is the insertion of a graphene sheet which, thanks to its large lateral conductivity and flatness can enhance the charge transport at the NWs array, and the yield of the whole device [111, 116]. On the other hand, the problem of NWs clustering can be solved by inserting a polymer between the NWs, which effectively separates them, avoiding short circuits [89].

## 1.5 Conclusions

The CAFM was invented in 1993 by M. P. Murrell and coauthors at the University of Cambridge, and it measures the local currents flowing between an ultrasharp tip and a sample. The CAFM is basically an AFM with three additional elements: a conductive probe tip, a voltage source, and a current/voltage preamplifier. The lateral resolution of the measurements is defined by the parameter $A_{eff}$, and it depends on the conductivity of the sample, the scanning parameters (e.g. contact force), the radius of the tip, and the environmental conditions in which the experiments are performed. The CAFM was initially used to measure the homogeneity and reliability of thin dielectrics, but later it expanded to many other fields of science. One of the main advantages compared to other nanoelectronic techniques is that the CAFM can simultaneously analyze the topography and conductivity of the sample scanned. This has allowed performing electromechanical measurements, such as inducing the movement of piezoelectric NWs and simultaneously collecting the current. New CAFM developments include multiprobe setups and their *in situ* combination with other techniques, which confirms a very promising panorama for CAFM based techniques.

## References

1 Bruker Dimension Icon Brochure, B068-RevB1, https://www.bruker.com/products/surface-analysis/atomic-force-microscopy/dimension-icon/learn-more.html (accessed 4 February 2016).
2 NanoWorld Nanoworld atomic force microscope probes catalogue, http://www.nanoworld.com/afm-probes-catalog (accessed 4 February 2016).
3 R.R.L. De Oliveira, D.A.C. Albuquerque, T.G.S. Cruz, F.M. Yamaji and F.L. Leite (2012) Measurement of the Nanoscale Roughness by Atomic Force Microscopy: Basic Principles and Applications 147–174. This is a chapter in the book: ATOMIC FORCE MICROSCOPY - IMAGING, MEASURING AND MANIPULATING SURFACES AT THE ATOMIC SCALE (Edited by Victor Bellitto). ISBN 978-953-51-0414-8. Published by InTech, in Janeza Trdine 9, 51000 Rijeka, Croatia (accessed 11 February 2017).
4 Zivkovic, J. (2013) AFM force spectroscopy of viral systems. PhD thesis. Radboud University.
5 Horcas, I., Fernández, R., Gómez-Rodríguez, J.M., Colchero, J., Gómez-Herrero, J., and Baro, A.M. (2007) A software for scanning probe microscopy and a tool for nanotechnology. *Rev. Sci. Instrum.*, **78**, 013705.

6 Tuning forks for ultrasensitive force spectroscopy measurements. Nanonics Imaging Ltd www.nanonics.co.il (accessed 13 February 2017).
7 Martin, Y., Williams, C.C., and Wickramasinghe, H.K. (1989) Atomic force microscope force mapping and profiling on an sub 100-a scale. *J. Appl. Phys.*, **61** (10), 4723–4729.
8 Sarid, D. and Elings, V. (1991) Review of scanning force microscopy. *J. Vac. Sci. Technol., B*, **9** (2), 431–437.
9 Israelachvili, J.N. (1992) *Intermolecular and Surface Forces*, Academic Press, London.
10 Frammelsberger, W., Benstetter, G., Kiely, J., and Stamp, R. (2007) C-AFM-based thickness determination of thin and ultra-thin SiO2 films by use of different conductive-coated probe tips. *Appl. Surf. Sci.*, **253** (7), 3615–3626.
11 Zhong, Q., Inniss, D., Kjoller, K., and Elings, V.B. (1993) Fractured polymer silica fiber surface studied by tapping mode Atomic-Force Microscopy. *Surf. Sci.*, **290**, 688–692.
12 Cappella, B. and Dietler, G. (1999) Force-distance curves by Atomic Force Microscope. *Surf. Sci. Rep.*, **34** (1-3), 1–104.
13 SPI supplies http://www.2spi.com/category/silver-paints-pastes (accessed 4 February 2016).
14 Lanza, M., Porti, M., Nafría, M., Aymerich, X., Whittaker, E., and Hamilton, B. (2010) Electrical resolution during conductive atomic force microscopy measurements under different environmental conditions and contact forces. *Rev. Sci. Instrum.*, **81**, 106110.
15 Rommel, M., Jambreck, J.D., Lemberger, M., Bauer, A.J., Frey, L., Murakami, K., Richter, C., and Weinzierl, P. (2013) Influence of parasitic capacitances on conductive AFM I-V measurements and approaches for its reduction. *J. Vac. Sci. Technol., B*, **31**, 01A108.
16 Yanev, V., Erlbacher, T., Rommel, M., Bauer, A.J., and Frey, L. (2009) Comparative study between conventional macroscopic IV techniques and advanced AFM based methods for electrical characterization of dielectrics at the nanoscale. *Microeletron. Eng.*, **86**, 1911–1914.
17 Lanza, M., Bayerl, A., Gao, T., Porti, M., Nafria, M., Jing, G., Zhang, Y., Liu, Z., and Duan, H. (2013) Graphene-coated atomic force microscope tips for reliable nanoscale electrical characterization. *Adv. Mater.*, **25**, 1440–1444.
18 Hui, F., Vajha, P., Shi, Y., Ji, Y., Duan, H., Padovani, A., Larcher, L., Li, X.R., Xu, J.J., and Lanza, M. (2016) Moving graphene devices from lab to market: advanced graphene-coated nanoprobes. *Nanoscale*, **8**, 8466–8473.
19 Diamond coated AFM tips, Nanoworld product catalogue, http://www.nanoworld.com/diamond-coated-afm-tips (accessed 13 February 2017).
20 Wen, Y.G. (2012) Multilayer graphene-coated atomic force microscopy tips for molecular junctions. *Adv. Mater.*, **24**, 3482.
21 Martin-Olmos, C., Rasool, H.M., Weiller, B.H., and Gimzewski, J.K. (2013) *ACS Nano*, **7**, 4164.
22 Gimzewski, J.K. (2013) Graphene MEMS: AFM probe performance improvement. *ACS Nano*, **7**, 4164.

**23** Shim, W., Brown, K.A., Zhou, X.Z., Rasin, B., Liao, X., and Mirkin, C.A. (2012) Multifunctional cantilever-free scanning probe arrays coated with multilayer graphene. *Proc. Natl. Acad. Sci. U.S.A.*, **109**, 18312.

**24** Lanza, M., Gao, T., Yin, Z.X., Zhang, Y.F., Liu, Z.F., Tong, Y.Z., Shen, Z.Y., and Duan, H.L. (2013) Nanogap based graphene coated AFM tips with high spatial resolution, conductivity and durability. *Nanoscale*, **5**, 10816.

**25** Bussmann, E. and Williams, C.C. (2004) Sub-10 nm lateral spatial resolution in scanning capacitance microscopy achieved with solid platinum probes. *Rev. Sci. Instrum.*, **75**, 422.

**26** Rocky Mountain Nanotechnology http://rmnano.com/ (accessed 4 February 2016).

**27** Hantschel, T., Demeulemeester, C., Eyben, P., Schulz, V., Richard, O., Bender, H., and Vandervorst, W. (2009) Conductive diamond tips with sub-nanometer electrical resolution for characterization of nanoelectronics device structures. *Phys. Status Solidi A*, **206**, 2077.

**28** Aguilera, L., Lanza, M., Porti, M., Grifoll, J., Nafría, M., and Aymerich, X. (2008) Improving the electrical performance of a conductive atomic force microscope with a logarithmic current-to-voltage converter. *Rev. Sci. Instrum.*, **79** (7), 073701.

**29** FEMTO http://www.femto.de/en/ (accessed 4 February 2016).

**30** Tiedje, T. and Brown, A. (1990) Performance limits for the scanning tunneling microscope. *J. Appl. Phys.*, **68** (2), 649–654.

**31** Instriuments http://www.ni.com/data-acquisition/ (accessed 4 February 2016).

**32** Ji, Y., Hui, F., Shi, Y., Iglesias, V., Lewis, D., Niu, J., Long, S., Liu, M., Hofer, A., Frammelsberger, W., Benstetter, G., Scheuermann, A., McIntyre, P.C., and Lanza, M. (2016) Characterization of the photocurrents generated by the laser of atomic force microscopes. *Rev. Sci. Instrum.*, **87**, 083703.

**33** Wang, Z.L. and Song, J.H. (2006) Piezoelectric nanogenerators based on zinc oxide nanowire arrays. *Science*, **312** (5771), 242–246.

**34** Muneer, A., Sang, A., Han, D., Hoang, T., Jongwan, J., and Yongho, S. (2011) Local conductance measurement of graphene layer using conductive atomic force microscopy. *J. Appl. Phys.*, **110**, 054307.

**35** Binnig, G., Quate, C.F., and Gerber, C. (1986) Atomic-force microscope. *Phys. Rev. Lett.*, **56**, 930–933.

**36** Murrell, M.P., Welland, M.E., O'Shea, S.J., Wong, T.M.H., Barnes, J.R., McKinnon, A.W., Heyns, M., and Verhaverbeke, S. (1993) Spatially resolved electrical measurements of SiO2 gate oxides using atomic force microscopy. *Appl. Phys. Lett.*, **62**, 786.

**37** O'Shea, S. J., Atta, R. M., Murrell, M. P., Welland, M. E. (1995) Conducting atomic-force microscopy study of silicon dioxide breakdown. *J. Vac. Sci. Technol., B*, **13** (5), 1945-1952.

**38** Ruskell, T.G., Workman, R.K., Chen, D., and Sarid, D. (1996) High resolution Fowler-Nordheim field emission maps of thin silicon oxide layers. *Appl. Phys. Lett.*, **68** (1), 93–95.

**39** Olbrich, A., Ebersberger, B., Boit, C. (1998) Nanoscale electrical characterization of thin oxides with conducting Atomic Force Microscopy.

Proceedings of the IEEE International Reliability Physics Symposium, 163-168.

40 Olbrich, A., Ebersberger, B., and Boit, C. (1998) Conducting atomic force microscopy for nanoscale electrical characterization of thin SiO2. *Appl. Phys. Lett.*, **73** (21), 3114–3116.

41 Olbrich, A., Ebersberger, B., Boit, C., Vancea, J., and Hoffmann, H. (1999) A new AFM-based tool for testing dielectric quality and reliability on a nanometer scale. *Microelectron. Reliab.*, **39** (6-7), 941–946.

42 Ebersberger, B., Benzinger, G. (1996) Thickness mapping of thin dielectrics with emission microscopy and conductive atomic microscopy for assessment of dielectrics reliability. Proceedings of the IEEE International Reliability Physics Symposium, 126-130.

43 Frammelsberger, W., Benstetter, G., Kiely, J., and Stamp, R. (2006) Thickness determination of thin and ultra-thin SiO2 films by CAFM IV-spectroscopy. *Appl. Surf. Sci.*, **252** (6), 2375–2388.

44 Polspoel, W. and Vandervorst, W. (2007) Evaluation of trap creation and charging in thin SiO2 using both SCM and C-AFM. *Microelectron. Eng.*, **84** (3), 495–500.

45 Nasyrov, K.A., Shaimeev, S.S., and Gritsenko, V.A. (2009) Trap-assisted tunneling hole injection in SiO2: experiment and theory. *J. Exp. Theor. Phys.*, **109** (5), 786–793.

46 Fiorenza, P., Polspoel, W., and Vandervorst, W. (2006) Conductive atomic force microscopy studies of thin SiO2 layer degradation. *Appl. Phys. Lett.*, **88** (22), 222104.

47 Wu, Y.L. and Lin, S.T. (2006) Two-trap-assisted tunneling model for post-breakdown I-V characteristics in ultrathin silicon dioxide. *IEEE Trans. Device Mater. Reliab.*, **6** (1), 75–80.

48 Pakes, C.I., Ramelow, S., Prawer, S., and Jamieson, D.N. (2004) Nanoscale electrical characterization of trap-assisted quasibreakdown fluctuations in SiO2. *Appl. Phys. Lett.*, **84** (16), 3142–3144.

49 Degraeve, R., Kaczer, B., Schuler, F., Lorenzini, M., Wellenkens, D., Hendrickx, P., Van Houdt, J., Haspeslagh, L., Tempel, G., Groeseneken, G. (2001) Statistical model for SILC and pre-breakdown current jumps in ultra-thin oxide layers. Proceedings of the IEEE International Electron Devices Meeting, 121–124.

50 Porti, M., Nafria, M., Aymerich, X., Olbrich, A., and Ebersberger, B. (2001) Electrical characterization of stressed and broken down SiO2 films at a nanometer scale using a conductive atomic force microscope. *J. Appl. Phys.*, **91** (4), 2071–2079.

51 Tan, T.T., Liu, Z.T., Tian, H., and Liu, W.T. (2010) Low voltage stress-induced leakage current in $HfO_2$ dielectric films. *Mater. Sci. Eng., B*, **171**, 159–161.

52 Ang, D.S., Ong, Y.C., O'Shea, S.J., Pey, K.L., Tung, C.H., and Kawanago, T. (2008) Polarity dependent breakdown of the high-k/$SiO_X$ gate stack: a phenomenological explanation by scanning tunneling microscopy. *Appl. Phys. Lett.*, **92** (19), 192904.

53 Lu, X.B., Zhang, X., Huang, R., Liu, H.B., Chen, Z.H., Zhou, H.W., Wang, X.P., Nguyen, B.Y., and Wang, C.Z. (2004) Effect of post-annealing on the physical and electrical properties of LaAlO3 gate dielectrics. *Proc. Int. Conf. Solid-State Integr. Circuits Technol.*, **1** (3), 419–422.

54 Lanza, M., Porti, M., Nafría, M., Aymerich, X., Benstetter, G., Lodermeier, E., Ranzinger, H., Jaschke, G., Teichert, S., Wilde, L., and Michalowski, P. (2009) Crystallization and silicon diffusion nanoscale effects on the electrical properties Of Al2O3 based devices. *Microelectron. Eng.*, **86** (7-9), 1921–1924.

55 Lanza, M., Porti, M., Nafría, M., Aymerich, X., Benstetter, G., Lodermeier, E., Ranzinger, H., Jaschke, G., Teichert, S., Wilde, L., and Michalowski, P. (2011) Conductivity and charge trapping after electrical stress in amorphous and polycristalline Al2O3 based devices studied with AFM related techniques. *IEEE Trans. Nanotechnol.*, **10** (2), 344–351.

56 Bayerl, A., Lanza, M., Porti, M., Nafría, M., Aymerich, X., and Benstetter, G. (2011) Nanoscale and device level gate conduction variability of high-k dielectrics-based metal-oxide-semiconductor structures. *IEEE Trans. Device Mater. Reliab.*, **11** (3), 495–501.

57 Lanza, M., Iglesias, V., Porti, M., Nafría, M., and Aymerich, X. (2011) Polyrystallization effects on the variability of the electrical properties of high-k dielectrics at the nanoscale. *Nanoscale Res. Lett.*, **6**, 108.

58 Bayerl, A., Lanza, M., Aguilera, L., Porti, M., Nafría, M., Aymerich, X., and De Gendt, S. (2013) Nanoscale and device level electrical behavior of ALD annealed Hf-based gate stacks grown with different precursors. *Microelectron. Reliab.*, **53** (6), 867–871.

59 Muenstermann, R., Menke, T., Dittmann, R., Mi, S., Jia, C.L., Park, D., and Mayer, J. (2010) Correlation between growth kinetics and nanoscale resistive switching properties of SrTiO3 thin films. *J. Appl. Phys.*, **108**, 124504.

60 Wu, Y.L., Lin, S.T., Chang, T.M., and Liou, J. (2007) Nanoscale bias-annealing effect in postirradiated thin silicon dioxide films observed by conductive atomic force microscopy. *IEEE Trans. Device Mater. Reliab.*, **7** (2), 351–355.

61 Wu, Y.L., Lin, S.T., Chang, T.M., and Liou, J. (2007) Reliability study of ultrathin oxide films subject to irradiation-then-stress treatment using conductive atomic force microscopy. *Microelectron. Reliab.*, **47** (2-3), 419–421.

62 Porti, M., Nafria, M., Gerardin, S., Aymerich, X., Cester, A., Paccagnella, A., and Ghidini, G. (2009) Implanted and irradiated SiO2/Si structure electrical properties at the nanoscale. *J. Vac. Sci. Technol., B*, **27** (1), 421–425.

63 Iglesias, V., Porti, M., Nafría, M., Aymerich, X., Dudek, P., Schroeder, T., and Bersuker, G. (2010) Correlation between the nanoscale electrical and morphological properties of crystallized hafnium oxide-based metal oxide semiconductor structures. *Appl. Phys. Lett.*, **97**, 262906.

64 Blasco, X., Nafría, M., Aymerich, X., and Vandervorst, W. (2005) Comparison of SiO2 and HfO2/SiO2 gate stacks electrical behaviour at a nanometer scale with CAFM. *Electron. Lett*, **41** (12), 719–721.

65 Wu, Y.L. and Lin, S.T. (2008) Breakdown spots propagation in ultrathin SiO2 films under repetitive ramped voltage stress using conductive atomic force microscopy. *J. Phys. Chem. Solids*, **69** (2-3), 470–474.

66 Lanza, M., Porti, M., Nafría, M., Aymerich, X., Whittaker, E., and Hamilton, B. (2010) UHV CAFM characterization of high-k dielectrics: effect of the technique resolution on the pre-and post-breakdown electrical measurements. *Microelectron. Reliab.*, **50** (9–11), 1312–1315.

67 Uppal, H.J., Bernardini, S., Efthymiou, E., Volkos, S.N., Dimoulas, A., Markevich, V., Hamilton, B. and Peaker, A.R. (2008) Nanoscale electrical characterization of ultra thin high-*k* dielectric MOS stacks: A conducting AFM study. *Materials Science in Semiconductor Processing*, **11**, 250–253.

68 Uppal, H.J., Mitrovic, I.Z., Hall, S., Hamilton, B., Markevich, V., and Peaker, A.R. (2009) Breakdown and degradation of ultrathin Hf-based (HfO2(x)(SiO 2)(1-x). *J. Vac. Sci. Technol., B*, **27** (1), 443–447.

69 Sire, C., Blonkiwski, S., Gordon, M.J., and Baron, T. (2007) Statistics of electrical breakdown field in HfO2 and SiO2 films from millimeter to nanometer length scales. *Appl. Phys. Lett.*, **91** (24), 242905.

70 Fiorenza, P., Lo Nigro, R., and Raineri, V. (2007) Breakdown kinetics at nanometer scale of innovative MOS devices by conductive atomic force microscopy. *Microelectron. Eng.*, **84** (3), 441–445.

71 Tung, C.H., Pey, K.L., Lin, W.H., and Radhakrishnan, M.K. (2002) Polarity-dependent dielectric breakdown-induced epitaxy (DBIE) in Si MOSFETs. *IEEE Electron Device Lett.*, **23** (9), 526–528.

72 Polspoel, W., Favia, P., Mody, J., Bender, H., and Vandervorst, W. (2009) Physical degradation of gate dielectrics induced by local electrical stress using conductive atomic force microscopy. *J. Appl. Phys.*, **106** (2), 024101.

73 Porti, M., Nafria, M., Blum, M.C., Aymerich, X., and Sadewasser, S. (2003) Atomic force microscope topographical artifacts after the dielectric breakdown of ultrathin SiO2 films. *Surf. Sci.*, **532–535**, 727–731.

74 Lanza, M., Zhang, K., Porti, M., Nafría, M., Shen, Z.Y., Liu, L.F., Kang, J.F., Gilmer, D., and Bersuker, G. (2012) Grain boundaries as preferential sites for resistive switching in the HfO2 resistive random access memory structures. *Appl. Phys. Lett.*, **100**, 123508.

75 Lanza, M. (2014) A review on resistive switching in high-k dielectrics: a nanoscale point of view using conductive atomic force microscope. *Materials*, **7**, 2155–2182.

76 Lee, G.H., Yu, Y.J., Lee, C., Dean, C., Shepard, K.L., Kim, P., and Hone, J. (2011) Electron tunneling through atomically flat and ultrathin hexagonal boron nitride. *Appl. Phys. Lett.*, **99**, 243114.

77 Ji, Y., Pan, C., Zhang, M., Long, S., Lian, X., Miao, F., Hui, F., Shi, Y., Larcher, L., Wu, E., and Lanza, M. (2016) Boron nitride as two dimensional dielectric: reliability and dielectric breakdown. *Appl. Phys. Lett.*, **108**, 012905.

78 Hattori, Y., Taniguchi, T., Watanabe, K., and Nagashio, K. (2015) Layer-by-layer dielectric breakdown of hexagonal boron nitride. *ACS Nano*, **9** (1), 916–921.

79 Piquemal-Banci, M., Galceran, R., Caneva, S., Martin, M.B., Weatherup, R.S., Kidambi, P.R., Bouzehouane, K., Xavier, S., Anane, A., Petroff, F., Fert, A., Robertson, J., Hofmann, S., Dlubak, B., and Seneor, P. (2016) Magnetic tunnel junctions with monolayer hexagonal boron nitride tunnel barriers. *Appl. Phys. Lett.*, **108**, 102404.

80 Britnell, L., Gorbachev, R.V., Jalil, R., Belle, B.D., Schedin, F., Katsnelson, M.I., Eaves, L., Morozov, S.V., Mayorov, A.S., Peres, N.M.R., Neto, A.H.C., Leist, J., Geim, A.K., Ponomarenko, L.A., and Novoselov, K.S. (2012) Electron tunneling through ultrathin boron nitride crystalline barriers. *Nano Lett.*, **12**, 1707–1710.

81 Sze, J.Y., Tay, B.K., Pakes, C.I., Jamieson, D.N., and Prawer, S. (2005) Conducting Ni nanoparticles in an ion-modified polymer. *J. Appl. Phys.*, **98**, 066101.

82 Cui, X.D., Primak, A., Zarate, X., Tomfohr, J., Sankey, O.F., Moore, A.L., Moore, T.A., Gust, D., Harris, G., and Lindsay, S.M. (2001) Reproducible measurement of single-molecule conductivity. *Science*, **294** (5542), 571–574.

83 Zhou, C., Kong, J., and Dai, H. (2000) Electrical measurements of individual semiconducting single-walled carbon nanotubes of various diameters. *Appl. Phys. Lett.*, **76**, 1597.

84 Vecchio, C., Sonde, S., Bongiorno, C., Rambach, M., Yakimova, R., Raineri, V., and Giannazzo, F. (2011) Nanoscale structural characterization of epitaxial graphene grown on off-axis 4H-SiC (0001). *Nanoscale Res. Lett.*, **6**, 269.

85 Giannazzo, F., Sonde, S., Rimini, E., and Raineri, V. (2011) Lateral homogeneity of the electronic properties in pristine and ion-irradiated graphene probed by scanning capacitance spectroscopy. *Nanoscale Res. Lett.*, **6**, 109.

86 Tan, S., Tang, Z., Liang, X., and Kotov, N.A. (2004) Resonance tunneling diode structures on CdTe nanowires made by conductive AFM. *Nano Lett.*, **4** (9), 1637–1641.

87 Lanza, M., Wang, Y., Gao, T., Bayer, A., Porti, M., Nafria, M., Zhou, Y., Jing, G., Zhang, Y., Liu, Z., Yu, D., and Duan, H. (2013) Electrical and mechanical performance of graphene sheets exposed to oxidative environments. *Nano Res.*, **6** (7), 485–495.

88 Howell, S.L., Padalkar, S., Yoon, K., Li, Q., Koleske, D.D., Wierer, J.J., Wang, G.T., and Lauhon, L.J. (2013) Spatial mapping of efficiency of GaN/InGaN nanowire array solar cells using scanning photocurrent microscopy. *Nano Lett.*, **13**, 5123–5128.

89 Pan, C., Hu, J., Grustan-Gutierrez, E., Hoang, M.T., Duan, H., Yvonnet, J., Mitrushchenkov, A., Chambaud, G., and Lanza, M. (2016) Suppression of nanowire clustering in hybrid energy harvesters. *J. Mater. Chem. C*, **4**, 3646.

90 ISI Web of Knowledge, Thomson Reuters www.webofscience.com.

91 Lanza, M., Porti, M., Nafria, M., Benstetter, G., Frammelsberger, W., Ranzinger, H., Lodermeier, E., and Jaschke, G. (2007) Influence of the manufacturing process on the electrical properties of thin (<4 nm) Hafnium based high-k stacks observed with CAFM. *Microelectron. Reliab.*, **47** (9-11), 1424–1428.

92 Okada, Y., Miyagi, M., Akahane, K., Kawabe, M., Shigekawa, H. (2002) Self-organized InGaAs quantum dots grown on GaAs (3 1 1) B substrate studied by conductive atomic force microscope technique *J. Cryst. Growth* **245**, 212–8.

93 Wu, S.J., Hopkins, T. http://nano.tm.agilent.com/apps_material/AN-ResiScope_5990-8413.PQ.pdf (accessed 21 July 2011).

94 Coll, M., Palau, A., Gonzalez-Rosillo, J.C., Gazquez, J., Obradors, X., and Puig, T. (2014) Integration of atomic layer deposition CeO2 thin films with functional complex oxides and 3D patterns. *Thin Solid Films*, **553**, 7–12.

95 Stahl, U., Yuan, C.W., Delozanne, A.L., and Tortonese, M. (1994) Atomic force microscope using piezoresistive cantilevers and combined with a scanning electron microscope. *Appl. Phys., Lett.*, **65** (22), 2878–2880.

96 Anderson, M.S. (2000) Locally enhanced Raman spectroscopy with an atomic force microscope. *Appl. Phys. Lett.*, **76** (21), 3130–3132.

97 Nanonics, http://www.nanonics.co.il/products/multiview-4000-system.

98 Sader, J.E. and Jarvis, S.P. (2004) Accurate formulas for interaction force and energy in frequency modulation force spectroscopy. *Appl. Phys. Lett.*, **84** (10), 1801–1803.

99 Nano verk http://www.nanowerk.com/atomic_force_microscope_manufacturers.php.

100 Leschkies, K.S., Divakar, R., Basu, J., Enache-Pommer, E., Boercker, J.E., Carter, C.B., Kortshagen, U.R., Norris, D.J., and Aydil, E.S. (2007) Photosensitization of zno nanowires with cdse quantum dots for photovoltaic devices. *Nano Lett.*, **7** (6), 1793–1798.

101 Wang, G., Wang, H., Ling, Y., Tang, Y., Yang, X., Fitzmorris, R.C., Wang, C., Zhang, J.Z., and Li, Y. (2011) Hydrogen-treated TiO2 nanowire arrays for photoelectrochemical water splitting. *Nano Lett.*, **11** (7), 3026–3033.

102 Xu, S., Lao, C.S., Weintraub, B., and Wang, Z.L. (2008) Density-controlled growth of aligned zno nanowire arrays by seedless chemical approach on smooth surfaces. *J. Mater. Res.*, **23**, 2072–2077.

103 Ge, X., Hong, K., Zhang, J., Liu, L.Q., and Xu, M.X.A. (2015) Controllable microwave-assisted hydrothermal method to synthesize ZnO nanowire arrays as recyclable photocatalyst. *Mater. Lett.*, **139**, 119–121.

104 San, X.G., Wang, G.S., Liang, B., Song, Y.M., Gao, S.Y., Zhang, J.S., and Meng, F.L. (2015) Catalyst-free growth of one-dimensional ZnO nanostructures on SiO2 substrate and in situ investigation of their H2 sensing properties. *J. Alloys Compd.*, **622**, 73–78.

105 Nam, G., Park, Y., Ji, L., Kim, B., Lee, S.H., Kim, D.Y., Kim, S., Kim, S.O., and Leem, J.Y. (2015) Facile synthesis and enhanced ultraviolet emission of zno nanorods prepared by vapor-confined face-to-face annealing. *ACS Appl. Mater. Interfaces*, **7**, 873–879.

106 Kar, J.P., Kim, S., Shin, B., Park, K.I., Ahn, K.J., Lee, W., Cho, J.H., and Myoung, J.M. (2010) Influence of sputtering pressure on morphological, mechanical and electrical properties of al-doped zno films. *Solid-State Electron.*, **54**, 1447–1450.

**107** Yang, M., Kim, H.C., and Hong, S.H. (2014) Growth of ZnO nanorods on fluorine-doped tin oxide substrate without catalyst by radio-frequency magnetron sputtering. *Thin Solid Films*, **573**, 79–83.

**108** Nicaise, S.M., Cheng, J.J., Kiani, A., Gradečak, S., and Berggren, K.K. (2015) Control of zinc oxide nanowire array properties with electron-beam lithography templating for photovoltaic applications. *Nanotechnology*, **26**, 075303.

**109** Khranovskyy, V. and Yakimova, R. (2012) Morphology engineering of ZnO nanostructures. *Physica B*, **407**, 1533–1537.

**110** Su, W.S., Chen, Y.F., Hsiao, C.L., and Tu, L.W. (2007) Generation of electricity in GaN nanorods induced by piezoelectric effect. *Appl. Phys. Lett.*, **90**, 063110.

**111** Lanza, M., Reguant, M., Zou, G., Lv, P., Li, H., Chin, R., Liang, H., Yu, D., Zhang, Y., Liu, Z., and Duan, H. (2014) High performance piezoelectric nanogenerators using two-dimensional flexible top electrodes. *Adv. Mater. Interfaces*, **1** (5), 1300101.

**112** Yang, T., Hertenberger, S., Morkötter, S., Abstreiter, G., and Koblmüller, G. (2012) Size, composition, and doping effects on In(Ga)As nanowire/Si tunnel diodes probed by conductive atomic force microscopy. *Appl. Phys. Lett.*, **101**, 233102.

**113** Hung, S.C. (2011) Generation of piezoelectricity by deflecting nanorods vertically on gan template. *J. Electrochem. Soc.*, **158** (12), H1265–H1269.

**114** Choi, D., Choi, M.Y., Choi, W.M., Shin, H.J., Park, H., Seo, J.S., and Park, J. (2006) Fully rollable transparent nanogenerators based on graphene electrodes. *Adv. Mater.*, **22**, 2187–2192.

**115** Xu, S., Wei, Y.G., Liu, J., Yang, R.S., and Wang, Z.L. (2008) Integrated multilayer nanogenerator fabricated using paired nanotip-to-nanowire brushes. *Nano Lett.*, **8**, 4027–4032.

**116** Kumar, B., Lee, K.Y., Park, H.K., Chae, S.J., Lee, Y.H., and Kim, S.W. (2011) Controlled growth of semiconducting nanowire, nanowall, and hybrid nanostructures on graphene for piezoelectric nanogenerators. *ACS Nano*, **5**, 4197–4204.